STRUCTURAL BIOLOGY

A kinase bioscavenger provides antibiotic resistance by extremely tight substrate binding

Stanislav S. Terekhov[1,2]*, Yuliana A. Mokrushina[1,2]*, Anton S. Nazarov[1]*, Alexander Zlobin[1,3]*, Arthur Zalevsky[1,3,4], Gleb Bourenkov[5], Andrey Golovin[1,3,4], Alexey Belogurov Jr.[1], Ilya A. Osterman[2,6], Alexandra A. Kulikova[7], Vladimir A. Mitkevich[7], Hua Jane Lou[8], Benjamin E. Turk[8], Matthias Wilmanns[5], Ivan V. Smirnov[1,2†], Sidney Altman[9,10†], Alexander G. Gabibov[1,2,11†]

Microbial communities are self-controlled by repertoires of lethal agents, the antibiotics. In their turn, these antibiotics are regulated by bioscavengers that are selected in the course of evolution. Kinase-mediated phosphorylation represents one of the general strategies for the emergence of antibiotic resistance. A new subfamily of AmiN-like kinases, isolated from the Siberian bear microbiome, inactivates antibiotic amicoumacin by phosphorylation. The nanomolar substrate affinity defines AmiN as a phosphotransferase with a unique catalytic efficiency proximal to the diffusion limit. Crystallographic analysis and multiscale simulations revealed a catalytically perfect mechanism providing phosphorylation exclusively in the case of a closed active site that counteracts substrate promiscuity. AmiN kinase is a member of the previously unknown subfamily representing the first evidence of a specialized phosphotransferase bioscavenger.

INTRODUCTION

Eons of evolution have forced living organisms to create killing agents to sufficiently eliminate the competing species. It required the extremely effective mechanisms of self-resistance to develop simultaneously, as well. These naturally evolved mechanisms are ubiquitous in all kingdoms ranging from microbes to advanced multicellular organisms. Competing with natural processes, researchers have devised artificial catalytic bioscavengers tailored by directed enzyme evolution to protect against the particularly toxic synthetic nerve agents (*1*–*3*). One of the most important lessons learned from the rational design and combinatorial approaches is the necessity of either of the two factors. It is either an extremely efficient binding to the substrate or a diffusion-limited catalytic efficiency of a bioscavenger to eliminate even the trace concentrations of a free toxin (*4*). The biodiversity of microbial communities is maintained by an intricate network of interactions between bacterial killers and the counteracting resistant bacteria competing with each other to colonize various ecological niches (*5*). Bacteria use the evolved antibiotic molecules to kill their competitors (*6*, *7*). In turn, selection pressure drives the evolution of enzymes that inactivate antibiotics; thus, they may be considered as natural catalytic bioscavengers detoxifying the potent killing agents (*8*). In contrast to the artificially designed bioscavengers, a broader substrate specificity is usually a more beneficial vector of selection in natural microbial communities, which is well documented in aminoglycoside (*9*) and macrolide (*10*) antibiotic resistance enzymes.

RESULTS

AmiN provides tight substrate binding

We report a unique bioscavenging kinase AmiN of *Bacillus pumilus* isolated from the oral microbiota of the Siberian bear (*Ursus arctos collaris*) by ultrahigh-throughput microfluidic droplet platform (*11*). Deep functional profiling of naïve bear microbiome for antibiotic activity enabled single-cell screening of antibiotic producers and resistant bacteria (*12*). Unlike common antibiotic resistance kinases, the new AmiN has an outstanding catalytic efficiency k_{cat}/K_M = $3.4 \pm 0.7 \times 10^8$ M^{-1} s^{-1} that is close to the diffusion limit toward its natural substrate, amicoumacin (Ami) (Fig. 1). This extraordinary catalytic efficiency originates from the tight Ami binding, which is

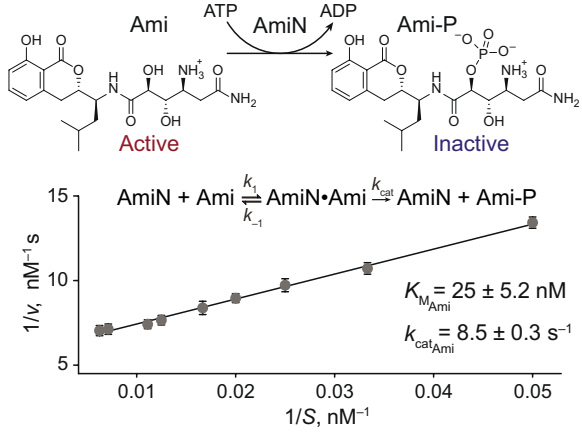

Fig. 1. Reaction (top) and Michaelis-Menten kinetics (bottom) of Ami phosphorylation by AmiN. Reaction rates were determined in triplicate at saturating ATP•Mg^{2+} concentrations, [ATP•Mg^{2+}] ≫ [Ami]. Kinetic constants for Ami are shown in the inset. Data represent means ± SD.

[1]Shemyakin-Ovchinnikov Institute of Bioorganic Chemistry of the Russian Academy of Sciences, Moscow, Russia. [2]Department of Chemistry, Lomonosov Moscow State University, Moscow, Russia. [3]Faculty of Bioengineering and Bioinformatics, Lomonosov Moscow State University, Moscow, Russia. [4]Sechenov First Moscow State Medical University, Institute of Molecular Medicine, Moscow, Russia. [5]European Molecular Biology Laboratory, Hamburg, Germany. [6]Skolkovo Institute of Science and Technology, Skolkovo, Russia. [7]Engelhardt Institute of Molecular Biology, Russian Academy of Sciences, Moscow, Russia. [8]Department of Pharmacology, Yale School of Medicine, New Haven, CT, USA. [9]Department of Molecular, Cellular and Developmental Biology, Yale University, New Haven, CT, USA. [10]Arizona State University, Tempe, AZ, USA. [11]Department of Life Sciences, Higher School of Economics, Moscow, Russia.
*These authors contributed equally to this work.
†Corresponding author. Email: smirnov@ibch.ru (I.V.S.); sidney.altman@yale.edu (S.A.); gabibov@ibch.ru, gabibov@gmail.com (A.G.G.)

one of the strongest among the enzymes using low–molecular weight substrates (*13*). The reaction rate follows the Michaelis-Menten kinetics at submicromolar Ami concentrations close to MIC (minimum inhibitory concentration) and displaying K_M of 25 ± 5.2 nM for Ami. These findings were in line with the observed K_d = 80 ± 25 nM for Ami complexed with AmiN in the presence of nonhydrolyzable adenosine triphosphate (ATP) analog adenylyl-imidodiphosphate (AMP-PNP) (see table S1). We suggest that the exceptional specificity of AmiN toward Ami is mediated by the mechanism of its operation based on the Ami-driven closure of the active site and the existence of an additional substrate-binding loop forming unique π-box structure. The latter has not been reported for other antibiotic kinases.

The biological function of AmiN is associated with Ami biosynthetic gene cluster containing a kinase-phosphatase cycle regulating the Ami antibiotic production and self-resistance. AmiN has numerous homologs in *Bacilli* (AmiN-like kinases) emphasizing its significance for its ecology and survival in the wild (*12*). AmiN and its homologs (hAmiN and YerI from Ami nonproducing *B. pumilus* and *Bacillus subtilis*, respectively) confer recombinant antibiotic resistance to Ami in bacteria, both Gram-positive and Gram-negative, as well as in mammalian cells (see table S2). The alternative natural targets of AmiN-like kinases could include antibiotics of *Bacilli*, like cognate antibiotic zwittermicin (*14*) and paenilamicin (*15*) having structural similarity.

A new kinase subfamily with unique structural features

AmiN-like kinases are clustered in a distinct subfamily (32 to 98% identity) with low amino acid sequence identity (9 to 24% identity) in comparison with other characterized enzymes (Fig. 2, A and B). Multiple sequence alignment uncovered a number of amino acid residues like E36, N37, K/R52, H/R58, Brenner's motif (H200, D202, and N207), H204, metal chelation site (D219, D221, and D222), and R286 conserved in AmiN-like and related subfamilies (Fig. 2C). Amino acid residues K3, E41, R59, K111, E158-L/Q161, and F218 represent the hallmarks of AmiN-like enzymes. The most prominent feature of AmiN-like enzymes is the additional substrate-binding loop N238-E248 (fig. S1). Refined crystal structures of AmiN (Fig. 3 and fig. S2, A and B) and hAmiN kinases (see table S3 and fig. S2, C and D) revealed that enzymes with the highest sequence identity and structural similarity are small-molecule kinases (fig. S3), specifically aminopropanol kinase [Protein Data Bank (PDB) ID: 6ef6; identity: 24%; root mean square deviation (RMSD): 3.2 Å], Ser/Thr protein kinase SrkA with an unidentified natural target (PDB ID: 1zyl; identity: 22%; RMSD: 3.0 Å), hexosamine kinase (PDB ID: 4ocu; identity: 14%; RMSD: 3.8 Å), and kinase with an unknown target (PDB ID: 2ppq; identity: 17%; RMSD: 3.6 Å).

The substrate specificities of AmiN and hAmiN show that AmiN is a bona fide Ami kinase with ~100-fold reduced activity toward Ami-like molecules, linear amino sugar *N*-methylglucamine, and C-terminal amidated peptide NS, while hAmiN is much more promiscuous (fig. S4). Other antibiotic kinases mediating the resistance toward aminoglycosides (PDB ID: 6fuc; identity: 12%; RMSD: 3.1 Å) and macrolides (PDB ID: 5igh; identity: 13%; RMSD: 4.0 Å) represent low sequence identity and structural similarity. AmiN kinase does not provide the resistance to aminoglycoside, macrolide, and tetracycline antibiotics (see table S4). AmiN shares a common protein kinase domain fold (Fig. 3); moreover, structurally similar protein kinase SrkA with an unidentified natural target phosphorylates myelin basic protein (MBP) in vitro (*16*). Therefore, to further understand the substrate specificity toward polypeptides, we studied phosphorylation of MBP and a combinatorial peptide library using radioactively labeled ATP (*17*). We identified that MBP and peptides P/I/R-S-W and Y-A-S mimicking an Ami sequence could be phosphorylated with AmiN (figs. S5 and S6). However, the protein kinase activity was more than two orders of magnitude lower in comparison with Ami (fig. S4).

The exceptional kinetic characteristics of AmiN motivated us to define the key features of its functioning. There is a marked difference between the unliganded AmiN and liganded AmiN in complex with Mg^{2+}, AMP-PNP, and Ami (Fig. 3A and fig. S2) arising from the closure of the AmiN active site. The AmiN closure is induced specifically by Ami rather than ATP (fig. S7) binding. The refined crystal structure of AmiN revealed common features with phosphotransferases—ATP-binding domain, Brenner's phosphotransferase motif (H200-D202-N207), and metal-binding site (Fig. 3B). AmiN also has a special substrate-binding loop mentioned before, which forms a cavity—π-box (complex π-stacking system organized by H204, H205, N238, W241, and Y242 amino acid residues) responsible

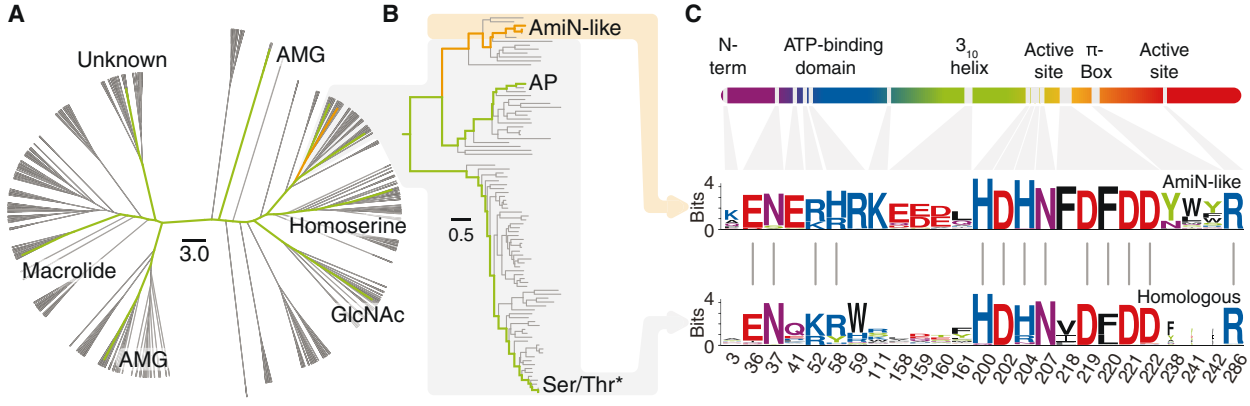

Fig. 2. Phylogeny of AmiN-like and other related kinases. (**A**) Phylogenetic tree of AmiN-related kinases from the APH (aminoglycoside phosphotransferase) family. Resolved crystal structures of the previously reported and AmiN/hAmiN kinases are shown by green and orange lines, respectively. Substrate specificity was assigned according to Protein Data Bank (PDB). (**B**) Homologs of AmiN-like subfamily. (**C**) Sequence logo featuring conserved amino acids of the AmiN-like, AP, and Ser/Thr*-like kinase subfamilies. AMG, aminoglycoside kinase; GlcNAc, *N*-acetylglucosamine kinase. AmiN-like subfamily was extended from the full set of APH family, *N* = 50. APH, aminoglycoside phosphotransferase PFAM (Protein Family database) family; AP, aminopropanol kinase; Ser/Thr*, protein kinase with an unidentified natural substrate.

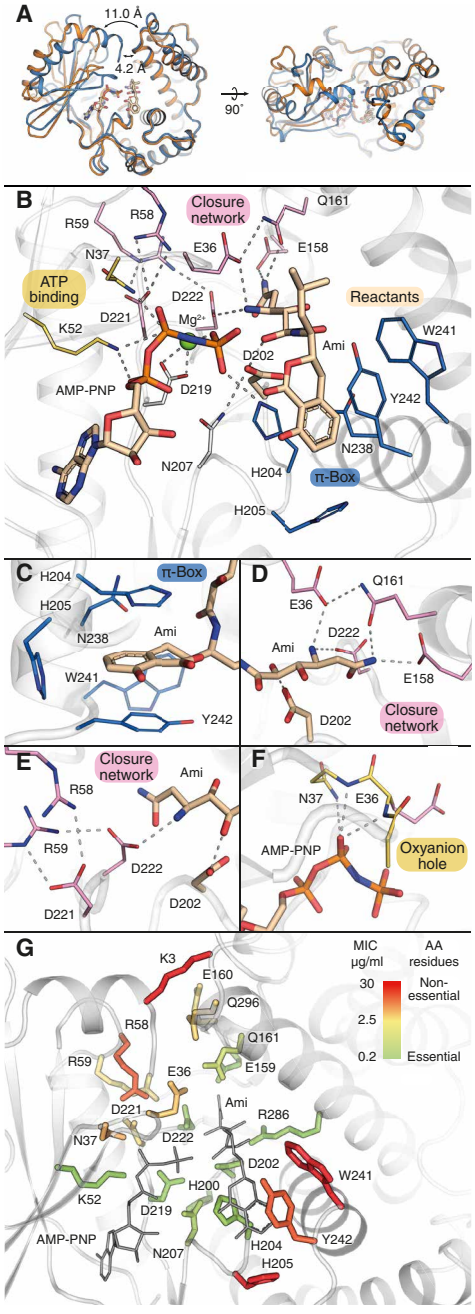

Fig. 3. Crystal structures of unliganded and substrate-bound AmiN kinase revealed active site architecture and marked conformational rearrangements upon substrate binding. (**A**) The overall closure of AmiN is mediated by substrate binding. Structural data for unliganded (orange) and liganded AmiN (blue) in complex with Mg^{2+} ion, AMP-PNP, and Ami. Distances are measured between Cα atoms of H2 and A297. Closure involves multiple modes of movement. (**B**) Overview of the AmiN active site. (**C**) π-Box (H204, H205, N238, W241, and Y242 amino acid residues) responsible for the high-affinity binding of Ami. (**D** to **F**) Intramolecular network of interactions between N-terminal ATP-binding domain and substrate-binding domain stabilized by hydrophilic part of Ami (mostly amine and terminal amide groups), formed by H-bonds and charge interactions between $NH_3^+{}_{Ami}$-E36-Q161-$CONH_{2Ami}$ (D) and Ami-D222D221-R58R59 (E) stabilizing closed AmiN structure. (F) Oxyanion hole playing an active role in phosphotransfer induced by the AmiN closure. Dashed lines indicate H-bonding and electrostatic interactions. (**G**) Amino acids (AA) essential for AmiN functioning. Color indicates the resistance of strains producing Ala-substituted variants of AmiN toward Ami.

for a high-affinity binding of Ami (Fig. 3C). The binding of Ami in the π-box itself is unable to induce AmiN closure, while it determines its outstanding specificity toward Ami-like molecules. Instead, AmiN closure is predetermined by stabilizing of an intramolecular network of interactions (fig. S8) between the N-terminal ATP-binding domain, substrate-binding domain, and the hydrophilic part of Ami (mostly the amine and terminal amide groups). This net is formed by H-bonds and charge interactions between $NH_3^+{}_{Ami}$-E36-Q161-$CONH_{2Ami}$ (Fig. 3D) and Ami-D222D221-R58R59 residues (Fig. 3E) stabilizing AmiN closed structure. The AmiN closure results in Ami positioning and convergence of ATP with OH_{Ami} residue and the formation of an oxyanion hole playing an active role in phosphotransfer (Fig. 3F). The specific amino acid residues essential for AmiN-based resistance that we associate with phosphotransfer (K52, D202, H204, N207, D219, D222, and R286) and AmiN closure (E36, R59, E159, Q161, and D221) were probed by a point mutagenesis (Fig. 3G and fig. S9). Single amino acid substitutions in the π-box do not lead to a complete loss of function, indicating the cooperativity in the complex π-stacking system.

The mechanism of phosphotransfer is mediated by active site closure

To clarify the mechanism underlying the AmiN functioning, we performed multiscale quantum mechanics (QM)/molecular mechanics (MM) simulations, which combine the precision of QM methods for the active center with the robustness of MM for the rest of the system (*18*). Molecular modeling revealed that AmiN in complex with ATP and Mg^{2+} exists in an open conformation, whereas a subsequent binding of Ami drives the enzyme active center closure (Fig. 4A). During this rearrangement (movie S1), the previously mentioned closure network (Fig. 3B) is formed. Positively charged N-terminal residues (the amino group of M1, H2, K3, and K6) also contribute to the process, specifically K3, which interacts with backbone oxygen at the C terminus of 270 to 290 alpha helix locking AmiN in the closed form (movie S1). Phosphorylation of Ami alters the conformational landscape in favor of open conformation, stimulating the product release. In line with this, kinetic and structural data demonstrated that Ca^{2+} ions, unlike Mg^{2+}, abolished Ami phosphorylation (fig. S10), forming a stable complex with the open hAmiN form (fig. S11). The open hAmiN is stabilized by Ca^{2+}-D221 chelation, inducing strong E36-R58 interaction; therefore, the oxyanion hole is not formed. Many different protein kinases are proposed to use two Mg^{2+} ions for optimal activity (*19*); however, at high Mg^{2+} concentrations, the product release becomes a rate-limiting step for them. Unlike these kinases, single Mg^{2+} is essential and sufficient for AmiN closure (Fig. 4A) and maximal activity (Fig. 5A), revealing ATP•Mg^{2+} complex to be AmiN substrate (Fig. 5B).

Furthermore, binding the second Mg^{2+} observed in the hAmiN•AMP-PNP•Ami complex (fig. S11) stabilizes the enzyme-product complex in the closed conformation (Fig. 5C), resulting in the enzyme inhibition observed at the increased Mg^{2+} concentrations (Fig. 5A). Unlike the case of two metal ion-binding protein kinases, the excess of ATP did not inhibit AmiN (fig. S12), stressing that the second Mg^{2+} is not necessary for catalysis. Michaelis constant for ATP measured in the presence of saturating Ami $K_M = 0.14 \pm 0.02$ mM (fig. S12) was similar to antibiotic kinases displaying K_M in the 0.01 to 1.9 mM range (*20*), *N*-acetylhexosamine kinase $K_M = 0.17$ mM (*21*), choline kinase $K_M = 0.35$ to 0.41 mM (*22*), and protein kinases displaying K_M in the 0.01 to 0.5 mM range (*23*).

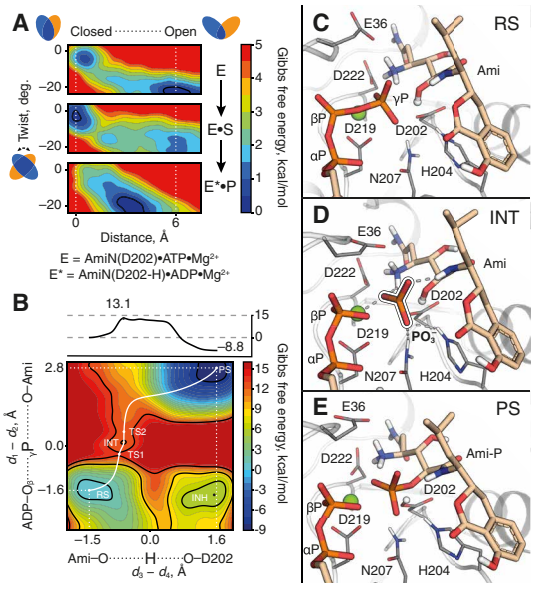

Fig. 4. Multiscale modeling elucidated atomistic details of both closure dynamics and phosphotransfer reaction proceeding via dissociative mechanism. (**A**) Free energy surfaces (FES) indicate the Ami-induced AmiN closure and opening induced by the reaction products. (**B**) FES of the reaction. Minimal barrier reaction pathway and stationary points along this way are shown. RS, reactant state; TS1 and TS2, transition states; INT, intermediate state; PS, product state; INH, inhibited state. FES along the minimal barrier reaction pathway is shown at the top. A detailed description of collective variables can be found in Materials and Methods. (**C** to **E**) Detailed representation of RS: AmiN-bound ATP, Ami, and Mg^{2+} ion (C); INT: AmiN-bound ADP, Ami, and stabilized PO_3^- (D); and PS: ADP and phosphorylated Ami (E). Phosphorus atoms are shown in orange, oxygen is shown in red, nitrogen is shown in blue, carbon is shown in gray, hydrogen is shown in white, and magnesium is shown in green. Transferred Ami proton is shown as a white sphere.

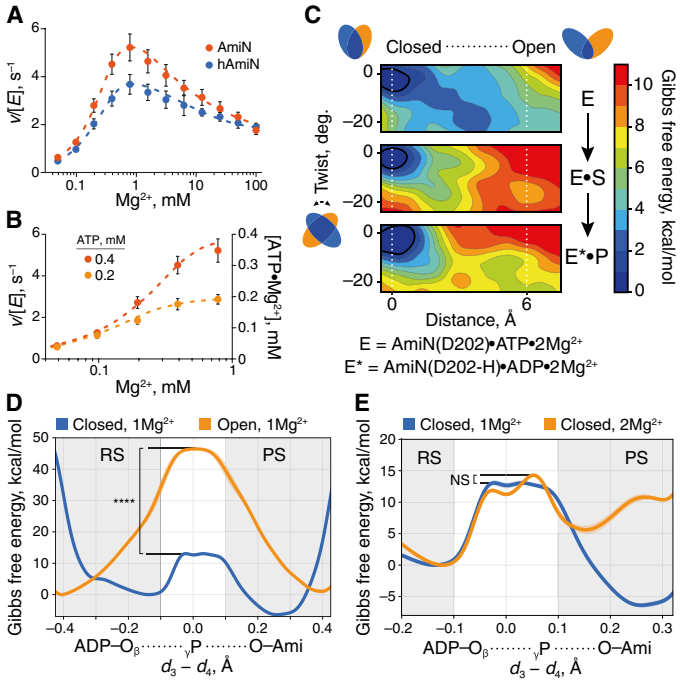

Fig. 5. AmiN-like kinases prefer single Mg^{2+} ion in the active site, indicating that the ATP•Mg^{2+} complex is an actual phosphate donor, while binding the second Mg^{2+} ion inhibits phosphotransfer by stabilizing the closed AmiN form. (**A**) The metal dependence of the reaction rate *v*/[*E*] illustrates that Mg^{2+} ions are essential for the phosphorylation of Ami by AmiN and hAmiN. The increased concentrations above the physiological level of ~1 mM result in the inhibition of the reaction. Reaction rates *v*/[*E*] were determined using 0.4 mM ATP in triplicate. Data represent means ± SD. (**B**) The reaction rate *v*/[*E*] of Ami phosphorylation (dots) depends on the concentration of the ATP•Mg^{2+} complex (dashed line) estimated using its K_d = 28.6 μM measured by Storer *et al.* (*34*). Reaction rates *v*/[*E*] were determined using 0.2 and 0.4 mM ATP in triplicate. Data represent means ± SD. (**C**) AmiN closure dynamics change drastically upon binding of the second Mg^{2+} ion to lock AmiN in the closed conformation. Free energy profiles of opening/closure dynamics are shown. AmiN is most effective in the closed form, and single Mg^{2+} ion is sufficient for phosphotransfer. (**D**) Comparison of the energy profiles of the phosphotransfer chemical stage in closed (blue) and open (orange) form of AmiN with a single Mg^{2+} ion. (**E**) Comparison of the energy profiles of phosphotransfer chemical stage proficiency with 1 Mg^{2+} (blue) or 2 Mg^{2+} (orange) ions in a closed form. SEM from five independent calculations is shown as a filled area. ****$P < 0.0001$; NS, not significant.

The QM/MM metadynamics indicated that the reaction proceeds through the dissociative mechanism (Fig. 4, B to E, and movie S1), and AmiN closure is essential for phosphotransfer (Fig. 5D). The estimated energetic barrier for open AmiN is substantially higher, indicating that the reaction rate in the closed form is more than eight orders of magnitude higher (Fig. 5D). At the first stage of the reaction, a gamma phosphate group is dissociated from the ATP molecule. A discrete stable intermediate state corresponds to the system with the dissociated metaphosphate anion and as yet the unactivated OH_{Ami} nucleophile of the substrate (Fig. 4D). The metaphosphate is stabilized by H-bonding with H204, N207, and internal NH_{Ami} amide and coordinated by Mg^{2+}. At the second step of the reaction, OH_{Ami} nucleophile is activated by proton transfer to D202, and P—O bond is simultaneously formed. The D202 residue is stabilized in the appropriate conformation for the proton transfer via interactions with N207 and R286. In line with the previous observations, QM simulations stressed that single Mg^{2+} ion is sufficient for phosphotransfer, while the second Mg^{2+} ion does not affect the rate of the reaction (Fig. 5E).

Metadynamics showed that phosphate transfer reaction is self-inhibited by the intramolecular Ami proton transfer from the positively charged $NH_3^+{}_{Ami}$ to the activated O-Ami reactive nucleophile of the substrate (see INH state on Fig. 4B and fig. S13A). The same $NH_3^+{}_{Ami}$ group is involved in proton exchange with the D222 amino acid residue (fig. S13B). The energetic barrier of 4.8 kcal/mol for the $NH_3^+{}_{Ami}$-D222 proton transfer was low as compared with the reaction barrier, which indicates that D222 protects $O^-{}_{Ami}$ nucleophile, being the essential amino acid residue for the phosphotransfer. We suggest that it is a common feature of *syn* alkanolamine kinases facing intramolecular substrate proton transfer (Fig. 2C).

DISCUSSION

The global spread of antibiotic resistance is one of the most urgent problems of humanity. The production of antibiotic-inactivating enzymes represents the particularly important molecular fingerprint of resistant strains. Hence, the detailed atomistic description of the molecular mechanisms of the operation of antibiotic kinases is essential for targeting antibiotic resistance by specific inhibitors and antibiotic analogs protected against the respective kinases. Here, we found a unique subfamily of AmiN-like kinases with an exceptional affinity for the substrate and provided its detailed phylogenetic,

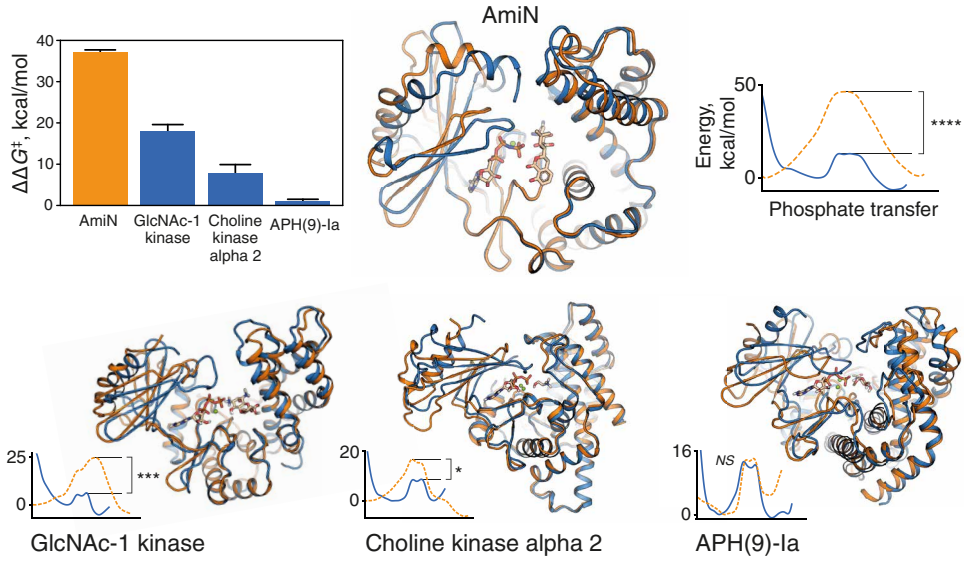

Fig. 6. The closed form provides more efficient phosphotransfer both in AmiN and related kinases. The energy profiles of the phosphotransfer chemical stage are presented for the closed (blue, solid line) and open (orange, dashed line) form of kinases. The difference in the reaction barrier between open and closed forms (bar plot, left inset) is presented with SEs calculated from three independent replicas. *$P < 0.05$, ***$P < 0.001$, and ****$P < 0.0001$.

structural, and functional description. The described mechanism of AmiN operation based on substrate-induced closure of the active site was observed for small-molecule kinases (*22*, *24*–*27*). Moreover, our multiscale QM/MM simulations revealed that the homologous enzymes—*N*-acetylhexosamine, spectinomycin, and choline kinase—display an enhanced phosphotransfer in a closed conformation as a result of a better gamma phosphate positioning toward a phosphoacceptor (Fig. 6). The kinetic restriction of substrate promiscuity stems from the described substrate-driven closure mechanism in the case of small-molecule kinases, while AmiN kinase represents the prime example. The novel AmiN kinase is a member of a previously unknown subfamily that evolved to phosphorylate a distinct substrate representing the first evidence of a specialized phosphotransferase bioscavenger. AmiN was initially annotated, automatically (*28*) as a homoserine kinase, and we consider that the number of misclassified antibiotic resistance enzymes with unique specificities and enzymes with unusual mechanisms (*29*) is very extensive. This substantially challenges the precise prediction of resistomes (*30*). The comprehensive understanding of the evolutionary landscapes and biodiversity of antibiotic resistance enzymes along with the detailed atomistic descriptions of the resistance mechanisms will improve both the prediction of antibiotic resistance threats and the development of targeted strategies to prevent them (*31*).

MATERIALS AND METHODS

Estimation of kinetic parameters of AmiN

Ami phosphorylation was performed in reaction buffer containing 50 mM Hepes-KOH (pH 7.5), 100 mM KCl, and 0.01% bovine serum albumin. Ami dependence of the reaction rate was measured at 30°C with 1 mM ATP, 1 mM $MgCl_2$, and 0.01 or 0.1 nM enzyme for 20 to 200 nM or 200 nM to 10 μM Ami, respectively. ATP dependence was measured with 30 μM to 10 mM ATP, 1 mM $MgCl_2$, 1 μM Ami, and 0.1 nM AmiN at 30°C. Mg^{2+} dependence was measured with 0.05 to 100 mM $MgCl_2$, 0.2 to 0.4 mM ATP, 1 μM Ami, and 0.1 nM AmiN at 30°C. Metal dependence for AmiN and hAmiN was measured using 10 mM ATP, 10 mM Me^{2+}, 1 μM Ami, and 0.1 nM enzyme at 30°C. Reaction mix was analyzed using Symmetry C18, 5 μm, 3.9 × 150 mm (Waters) reversed-phase high-performance liquid chromatography (HPLC) column; buffer A [10 mM NH_4OAc (pH 5.0) and 5% ACN], buffer B [10 mM NH_4OAc (pH 5.0) and 80% ACN]; flow rate: 1 ml/min: gradient: 0 to 1 min (0% B), 1 to 11 min (0 to 67% B), and 11 to 11.5 min (67 to 100% B) on Chromaster HPLC System (Hitachi) as described previously (*12*). Amicoumacin and its phosphorylated product were monitored using Chromaster Fluorescence Detector (λ_{ex} = 317 nm and λ_{em} = 469 nm). Reaction rates were determined in triplicate. K_M and k_{cat} constants were calculated using the Michaelis-Menten kinetics at 20 to 200 nM Ami concentrations, assuming [ATP•Mg^{2+}] >> [Ami]. Kinetic constants were determined using Prism 7 (GraphPad) software. Data represent means ± SD.

Estimation of thermodynamic parameters of substrate binding

The thermodynamic parameters of binding of ATP/adenosine diphosphate (ADP)/Ami to AmiN and Ami/phosphorylated Ami to AmiN-nucleotide complexes were measured by isothermal titration calorimetry (ITC) using a MicroCal iTC200 calorimeter (GE Healthcare Life Sciences, USA) at 25°C in 20 mM bis-tris-propane-HCl, 50 mM KCl, 2.5% glycerol, and 2 mM $MgCl_2$ (or 2 mM $CaCl_2$) (pH 8.5). Aliquots (2.5 μl) of ligands were injected into a 0.2-ml cell containing the protein solution to achieve a complete binding isotherm. Protein solution (20 μM) in the cell and 250 μM ligand in the titrant syringe were used for each experiment. In the case of AmiN-nucleotide complexes, samples contained 20 μM protein and 50 μM AMP-PNP or ADP. The heat of dilution was measured by injection of the ligand into the buffer solution; the values obtained were subtracted from the heat of reaction to calculate the effective heat of binding. All measurements were done in triplicate. The resulting titration curves were fitted and analyzed using the Microcal Origin software, assuming one set of binding sites. Affinity constants (K_a) and enthalpy variations (ΔH) were determined, and entropy variations (ΔS) were calculated from the equation

$$\Delta G = -RT\ln K_a = \Delta H - T\Delta S$$

Crystallization of AmiN and hAmiN

AmiN and hAmiN crystals were grown at 19°C using the hanging drop vapor diffusion method. All samples were centrifuged at 16,000*g* for 10 min before crystallization. Native AmiN crystals were produced by combining 1 μl of protein with a concentration of 25 mg/ml and an equal volume of crystallization solution containing 0.1 M tris-HCl (pH 8.5), 2.5 to 2.65 M ammonium sulfate. AmiN in complex with ATP was crystallized under similar conditions with preliminary mixing of protein and ATP (added to a final concentration of 10 mM). In both cases, the crystals appeared within 12 to 24 hours. For crystallization of AmiN in complex with AMP-PNP, Mg^{2+}, and Ami, protein with a final concentration of 70 mg/ml (1.8 mM) was mixed with AMP-PNP, Ami, and $MgCl_2$ to a final concentration of 10, 3.6, and 20 mM, respectively. Crystals were obtained by mixing 1 μl of protein complex solution and 1 μl of reservoir solution containing 0.1 M tris-HCl (pH 8.5), 1.1 M LiCl, and 27.5% (w/v) polyethylene glycol (PEG) 4000. These crystals appeared within 3 to 5 days. In the case of hAmiN, protein with a final concentration of 40 mg/ml (1 mM) was mixed with AMP-PNP, Ami, and $MgCl_2$ or $CaCl_2$ to a final concentration of 2.2, 2, and 20 mM, respectively. hAmiN crystals were produced using 1 μl of protein complex solution and 1 μl of the crystallization solution containing 0.1 M MES (pH 6.5), 0.2 M sodium acetate, and 27 to 29% (w/v) PEG 2000 MME (monomethyl ether). Crystals appeared within 2 to 3 days.

Estimation of AmiN and hAmiN activity toward different substrates

AmiN and hAmiN activity toward a broad range of substrates was measured using Fluorometric Universal Kinase Assay Kit ab138879 (Abcam) on the basis of quantification of released ADP. The following substrates listed below were used: *N*-acetylglucosamine, glucosamine 6-phosphate, glucose, sucrose, sorbitol, glycerol, 2-amino-2-(hydroxymethyl)propane-1,3-diol (tris), serine, threonine, tyrosine, MBP, YAS-NH_2, YLS-NH_2, YS-NH_2, PSW-NH_2, choline, aminomethyl propanol, 3-dimethylamino-1-propanol, *N*-methyl-D-glucamine, glucosamine, galactosamine, kanamycin, ethanolamine, 3-amino-1-propanol, 4-amino-1-butanol, NS-NH_2, Ac-PSW-NH_2, Ac-ISW-NH_2, Ac-RSW-NH_2, NSL-NH_2, NSLY-NH_2, SL-NH_2, and SLY-NH_2. The ADP release was assayed in 50 mM Hepes-KOH (pH 7.5), 100 mM KCl, 0.1 mM ATP, 10 mM $MgCl_2$, and 10 mM substrates using 0.2 μM enzymes. Reaction mixtures were incubated at 30°C for 30 min and assayed with ab138879 (Abcam) kit in kinetic mode using the Varioskan Flash reader (Thermo Fisher Scientific) according to the manufacturer's instructions. The estimated release of ADP was calculated using the calibration curve, and background ADP released in the substrate-free reaction was subtracted. Reaction rates $v/[E]$ were determined in triplicate and analyzed by multiple *t* tests using Prism 7 (GraphPad) software.

Simulation of opening/closure dynamics

Opening/closure free energy profiles were reconstructed in two dimensions with metadynamics implemented in Plumed 2.5.1 (*32*). The first collective variable (CV) corresponded to the interdomain distance, and the second corresponded to the relative twist of domains (fig. S14). To calculate the interdomain distance as the first CV, domain centers were designated as centers of mass of Cα atoms only, where the left domain is demarcated as a set of residues 1 to 55 and 84 to 110 and the right domain is demarcated as a set of residues 156 to 189 and 281 to 320. This CV was subsequently centered at the value corresponding to the closed AmiN kinase (30 Å). The second CV, being the twist of protein fold, was described as a torsion angle between Cα atoms of residues 46, 4, 302, and 184 and centered at the value for closed AmiN kinase (107°). Well-tempered metadynamics simulation was performed in parallel by 15 walkers, depositing a Gaussian potential with an initial height of 0.25 kJ/mol and a width of 0.025 nm, 0.025 rad each 1000 steps with time step of 1 fs. Bias factor was set to 9. Profile was sampled for 10 ns per walker.

Simulation of phosphate transfer reaction

Reaction free energy profiles were reconstructed in one and two dimensions with metadynamics. For one-dimensional profiles, collective variable was designed as

$$\mathrm{CV}_1 = d_1 - d_2 \text{ where}$$

$$d_1 = \min_i\left(d\left(O_\beta^i - P_\gamma\right)\right) \text{ and}$$

$$d_2 = d(P_\gamma - O_{\mathrm{Ami}})$$

to capture the phosphorus transfer process. Here, O_β^i stands for each of three beta-oxygens of ATP. For two-dimensional description, second variable was added as

$$\mathrm{CV}_2 = d_3 - d_4 \text{ where}$$

$$d_3 = d(O_{\mathrm{Ami}} - H_{\mathrm{Ami}}) \text{ and}$$

$$d_4 = \min_j\left(d(O_{\mathrm{D202}}^j - H_{\mathrm{Ami}})\right)$$

to explicitly capture the proton transfer process. Here, O_{D202}^j stands for each of two carboxylate oxygens of D202. Well-tempered metadynamics simulation (*33*) was performed in parallel by 28 walkers, depositing a Gaussian potential with an initial height of 2.0 kJ/mol and a width of 0.005 nm in each direction each 100 steps with time step 0.2 fs. Bias factor was set to 20. Profile was sampled for 20 ps per walker.

Simulation of Ami proton transfer

Free energy profiles of proton transfer from Ami-NH_3^+ to either E36 or D222 were reconstructed with metadynamics along single variable

$$D = \min_{i,j}\left(d(H_i - O_j)\right)$$

where H_i is any of three protons on the NH_3^+ group and O_j is any of two carboxylate oxygens. Well-tempered metadynamics simulation was performed in parallel by eight walkers, depositing a Gaussian potential with an initial height of 1.0 kJ/mol and a width of 0.005 nm each 50 steps with time step of 0.2 fs. Bias factor was set to 15. Profile was sampled for 20 ps per walker. Crystal structures, initial coordinates for simulations, simulations settings, and metadynamics parameters are available online at https://vsb.fbb.msu.ru/share/amin_kinase/. For more detailed information, please refer to Supplementary Materials and Methods.

SUPPLEMENTARY MATERIALS

Supplementary material for this article is available at http://advances.sciencemag.org/cgi/content/full/6/26/eaaz9861/DC1

View/request a protocol for this paper from *Bio-protocol*.

REFERENCES AND NOTES

1. R. D. Gupta, M. Goldsmith, Y. Ashani, Y. Simo, G. Mullokandov, H. Bar, M. Ben-David, H. Leader, R. Margalit, I. Silman, J. L. Sussman, D. S. Tawfik, Directed evolution of hydrolases for prevention of G-type nerve agent intoxication. *Nat. Chem. Biol.* **7**, 120–125 (2011).
2. I. Cherny, P. Greisen Jr., Y. Ashani, S. D. Khare, G. Oberdorfer, H. Leader, D. Baker, D. S. Tawfik, Engineering v-type nerve agents detoxifying enzymes using computationally focused libraries. *ACS Chem. Biol.* **8**, 2394–2403 (2013).
3. I. V. Smirnov, A. V. Golovin, S. D. Chatziefthimiou, A. V. Stepanova, Y. Peng, O. I. Zolotareva, A. A. Belogurov Jr., I. N. Kurkova, N. A. Ponomarenko, M. Wilmanns, G. M. Blackburn, A. G. Gabibov, R. A. Lerner, Robotic QM/MM-driven maturation of antibody combining sites. *Sci. Adv.* **2**, e1501695 (2016).
4. B. C. Geyer, L. Kannan, P.-E. Garnaud, C. A. Broomfield, C. L. Cadieux, I. Cherni, S. M. Hodgins, S. A. Kasten, K. Kelley, J. Kilbourne, Z. P. Oliver, T. C. Otto, I. Puffenberger, T. E. Reeves, N. Robbins II, R. R. Woods, H. Soreq, D. E. Lenz, D. M. Cerasoli, T. S. Mor, Plant-derived human butyrylcholinesterase, but not an organophosphorous-compound hydrolyzing variant thereof, protects rodents against nerve agents. *Proc. Natl. Acad. Sci. U.S.A.* **107**, 20251–20256 (2010).
5. E. D. Kelsic, J. Zhao, K. Vetsigian, R. Kishony, Counteraction of antibiotic production and degradation stabilizes microbial communities. *Nature* **521**, 516–519 (2015).
6. M. E. Hibbing, C. Fuqua, M. R. Parsek, S. B. Peterson, Bacterial competition: Surviving and thriving in the microbial jungle. *Nat. Rev. Microbiol.* **8**, 15–25 (2010).
7. S. Altman, Antibiotics present and future. *FEBS Lett.* **588**, 1–2 (2014).
8. P. Masson, F. Nachon, Cholinesterase reactivators and bioscavengers for pre- and post-exposure treatments of organophosphorus poisoning. *J. Neurochem.* **142**, 26–40 (2017).
9. S. J. Caldwell, A. M. Berghuis, Plasticity of aminoglycoside binding to antibiotic kinase APH(2″)-Ia. *Antimicrob. Agents Chemother.* **62**, e00202–e00218 (2018).
10. A. C. Pawlowski, P. J. Stogios, K. Koteva, T. Skarina, E. Evdokimova, A. Savchenko, G. D. Wright, The evolution of substrate discrimination in macrolide antibiotic resistance enzymes. *Nat. Commun.* **9**, 112 (2018).
11. S. S. Terekhov, I. V. Smirnov, A. V. Stepanova, T. V. Bobik, Y. A. Mokrushina, N. A. Ponomarenko, A. A. Belogurov Jr., M. P. Rubtsova, O. V. Kartseva, M. O. Gomzikova, A. A. Moskovtsev, A. S. Bukatin, M. V. Dubina, E. S. Kostryukova, V. V. Babenko, M. T. Vakhitova, A. I. Manolov, M. V. Malakhova, M. A. Kornienko, A. V. Tyakht, A. A. Vanyushkina, E. N. Ilina, P. Masson, A. G. Gabibov, S. Altman, Microfluidic droplet platform for ultrahigh-throughput single-cell screening of biodiversity. *Proc. Natl. Acad. Sci. U.S.A.* **114**, 2550–2555 (2017).
12. S. S. Terekhov, I. V. Smirnov, M. V. Malakhova, A. E. Samoilov, A. I. Manolov, A. S. Nazarov, D. V. Danilov, S. A. Dubiley, I. A. Osterman, M. P. Rubtsova, E. S. Kostryukova, R. H. Ziganshin, M. A. Kornienko, A. A. Vanyushkina, O. N. Bukato, E. N. Ilina, V. V. Vlasov, K. V. Severinov, A. G. Gabibov, S. Altman, Ultrahigh-throughput functional profiling of microbiota communities. *Proc. Natl. Acad. Sci. U.S.A.* **115**, 9551–9556 (2018).
13. A. Bar-Even, E. Noor, Y. Savir, W. Liebermeister, D. Davidi, D. S. Tawfik, R. Milo, The moderately efficient enzyme: Evolutionary and physicochemical trends shaping enzyme parameters. *Biochemistry* **50**, 4402–4410 (2011).
14. B. M. Kevany, D. A. Rasko, M. G. Thomas, Characterization of the complete zwittermicin a biosynthesis gene cluster from *Bacillus cereus*. *Appl. Environ. Microbiol.* **75**, 1144–1155 (2009).
15. S. Müller, E. Garcia-Gonzalez, A. Mainz, G. Hertlein, N. C. Heid, E. Mösker, H. van den Elst, H. S. Overkleeft, E. Genersch, R. D. Süssmuth, Paenilamicin: Structure and biosynthesis of a hybrid nonribosomal peptide/polyketide antibiotic from the bee pathogen *Paenibacillus larvae*. *Angew. Chem. Int. Ed. Engl.* **53**, 10821–10825 (2014).
16. A. Dorsey-Oresto, T. Lu, M. Mosel, X. Wang, T. Salz, K. Drlica, X. Zhao, YihE Kinase is a central regulator of programmed cell death in bacteria. *Cell Rep.* **3**, 528–537 (2013).
17. J. E. Hutti, E. T. Jarrell, J. D. Chang, D. W. Abbott, P. Storz, A. Toker, L. C. Cantley, B. E. Turk, A rapid method for determining protein kinase phosphorylation specificity. *Nat. Methods* **1**, 27–29 (2004).
18. A. Warshel, Multiscale modeling of biological functions: From enzymes to molecular machines (Nobel Lecture). *Angew. Chem. Int. Ed. Engl.* **53**, 10020–10031 (2014).
19. D. M. Jacobsen, Z.-Q. Bao, P. O'Brien, C. L. Brooks III, M. A. Young, Price to be paid for two-metal catalysis: Magnesium ions that accelerate chemistry unavoidably limit product release from a protein kinase. *J. Am. Chem. Soc.* **134**, 15357–15370 (2012).
20. T. Shakya, G. D. Wright, Nucleotide selectivity of antibiotic kinases. *Antimicrob. Agents Chemother.* **54**, 1909–1913 (2010).
21. M. Nishimoto, M. Kitaoka, Identification of *N*-acetylhexosamine 1-kinase in the complete lacto-*N*-biose I/galacto-*N*-biose metabolic pathway in *Bifidobacterium longum*. *Appl. Environ. Microbiol.* **73**, 6444–6449 (2007).
22. E. Malito, N. Sekulic, W. C. S. Too, M. Konrad, A. Lavie, Elucidation of human choline kinase crystal structures in complex with the products ADP or phosphocholine. *J. Mol. Biol.* **364**, 136–151 (2006).
23. A. F. Rudolf, T. Skovgaard, S. Knapp, L. J. Jensen, J. Berthelsen, A comparison of protein kinases inhibitor screening methods using both enzymatic activity and binding affinity determination. *PLOS ONE* **9**, e98800 (2014).
24. G. E. Schulz, C. W. Müller, K. Diederichs, Induced-fit movements in adenylate kinases. *J. Mol. Biol.* **213**, 627–630 (1990).
25. S. D. Lahiri, P.-F. Wang, P. C. Babbitt, M. J. McLeish, G. L. Kenyon, K. N. Allen, The 2.1 Å structure of *Torpedo californica* creatine kinase complexed with the ADP-Mg^{2+}–NO_3^-–creatine transition-state analogue complex†,‡. *Biochemistry* **41**, 13861–13867 (2002).
26. K.-C. Wang, S.-Y. Lyu, Y.-C. Liu, C.-Y. Chang, C.-J. Wu, T.-L. Li, Insights into the binding specificity and catalytic mechanism of *N*-acetylhexosamine 1-phosphate kinases through multiple reaction complexes. *Acta Crystallogr. D Biol. Crystallogr.* **70**, 1401–1410 (2014).
27. D. H. Fong, C. T. Lemke, J. Hwang, B. Xiong, A. M. Berghuis, Structure of the antibiotic resistance factor spectinomycin phosphotransferase from *Legionella pneumophila*. *J. Biol. Chem.* **285**, 9545–9555 (2010).
28. T. Seemann, Prokka: Rapid prokaryotic genome annotation. *Bioinformatics* **30**, 2068–2069 (2014).
29. P. J. Stogios, G. Cox, P. Spanogiannopoulos, M. C. Pillon, N. Waglechner, T. Skarina, K. Koteva, A. Guarné, A. Savchenko, G. D. Wright, Rifampin phosphotransferase is an unusual antibiotic resistance kinase. *Nat. Commun.* **7**, 11343 (2016).
30. K. J. Forsberg, A. Reyes, B. Wang, E. M. Selleck, M. O. A. Sommer, G. Dantas, The shared antibiotic resistome of soil bacteria and human pathogens. *Science* **337**, 1107–1111 (2012).
31. T. S. Crofts, A. J. Gasparrini, G. Dantas, Next-generation approaches to understand and combat the antibiotic resistome. *Nat. Rev. Microbiol.* **15**, 422–434 (2017).
32. G. A. Tribello, M. Bonomi, D. Branduardi, C. Camilloni, G. Bussi, PLUMED 2: New feathers for an old bird. *Comput. Phys. Commun.* **185**, 604–613 (2014).
33. A. Barducci, G. Bussi, M. Parrinello, Well-tempered metadynamics: A smoothly converging and tunable free-energy method. *Phys. Rev. Lett.* **100**, 020603 (2008).
34. A. C. Storer, A. Cornish-Bowden, Concentration of $MgATP^{2-}$ and other ions in solution. Calculation of the true concentrations of species present in mixtures of associating ions. *Biochem. J.* **159**, 1–5 (1976).
35. F. W. Studier, Protein production by auto-induction in high-density shaking cultures. *Protein Expr. Purif.* **41**, 207–234 (2005).
36. M. Cianci, G. Bourenkov, G. Pompidor, I. Karpics, J. Kallio, I. Bento, M. Roessle, F. Cipriani, S. Fiedler, T. R. Schneider, P13, the EMBL macromolecular crystallography beamline at the low-emittance PETRA III ring for high- and low-energy phasing with variable beam focusing. *J. Synchrotron Radiat.* **24**, 323–332 (2017).
37. G. M. Sheldrick, Experimental phasing with *SHELXC/D/E*: Combining chain tracing with density modification. *Acta Crystallogr. D Biol. Crystallogr.* **66**, 479–485 (2010).
38. T. Pape, T. R. Schneider, *HKL2MAP*: A graphical user interface for macromolecular phasing with *SHELX* programs. *J. Appl. Cryst.* **37**, 843–844 (2004).
39. V. S. Lamzin, A. Perrakis, K. S. Wilson, in *International Tables for Crystallography*, T. H. C. P. Brock, H. Wondratschek, U. Müller, U. Shmueli, E. Prince, A. Authier, V. Kopský, D. B. Litvin, E. Arnold, D. M. Himmel, M. G. Rossmann, S. R. Hall, B. McMahon, E. Arnold, D. M. Himmel, M. G. Rossmann, Eds. (2012) pp. 525–528.
40. A. Vagin, A. Teplyakov, Molecular replacement with *MOLREP*. *Acta Cryst.* **66**, 22–25 (2010).
41. P. Emsley, K. Cowtan, *Coot*: Model-building tools for molecular graphics. *Acta Crystallogr. D Biol. Crystallogr.* **60**, 2126–2132 (2004).
42. G. N. Murshudov, P. Skubák, A. A. Lebedev, N. S. Pannu, R. A. Steiner, R. A. Nicholls, M. D. Winn, F. Long, A. A. Vagin, *REFMAC5* for the refinement of macromolecular crystal structures. *Acta Crystallogr. D Biol. Crystallogr.* **67**, 355–367 (2011).
43. C. J. Miller, H. J. Lou, C. Simpson, B. van de Kooij, B. H. Ha, O. S. Fisher, N. L. Pirman, T. J. Boggon, J. Rinehart, M. B. Yaffe, R. Linding, B. E. Turk, Comprehensive profiling of the STE20 kinase family defines features essential for selective substrate targeting and signaling output. *PLOS Biol.* **17**, e2006540 (2019).
44. S. Mirarab, N. Nguyen, S. Guo, L.-S. Wang, J. Kim, T. Warnow, PASTA: Ultra-large multiple sequence alignment for nucleotide and amino-acid sequences. *J. Comput. Biol.* **22**, 377–386 (2015).
45. K. Katoh, D. M. Standley, MAFFT multiple sequence alignment software version 7: Improvements in performance and usability. *Mol. Biol. Evol.* **30**, 772–780 (2013).
46. L.-T. Nguyen, H. A. Schmidt, A. von Haeseler, B. Q. Minh, IQ-TREE: A fast and effective stochastic algorithm for estimating maximum-likelihood phylogenies. *Mol. Biol. Evol.* **32**, 268–274 (2014).
47. S. Q. Le, O. Gascuel, An improved general amino acid replacement matrix. *Mol. Biol. Evol.* **25**, 1307–1320 (2008).

48. J. Soubrier, M. Steel, M. S. Y. Lee, C. der Sarkissian, S. Guindon, S. Y. W. Ho, A. Cooper, The influence of rate heterogeneity among sites on the time dependence of molecular rates. *Mol. Biol. Evol.* **29**, 3345–3358 (2012).
49. S. Kalyaanamoorthy, B. Q. Minh, T. K. F. Wong, A. von Haeseler, L. S. Jermiin, ModelFinder: Fast model selection for accurate phylogenetic estimates. *Nat. Methods* **14**, 587–589 (2017).
50. D. T. Hoang, O. Chernomor, A. von Haeseler, B. Q. Minh, L. S. Vinh, UFBoot2: Improving the ultrafast bootstrap approximation. *Mol. Biol. Evol.* **35**, 518–522 (2017).
51. G. E. Crooks, G. Hon, J.-M. Chandonia, S. E. Brenner, WebLogo: A sequence logo generator. *Genome Res.* **14**, 1188–1190 (2004).
52. A. Larsson, AliView: A fast and lightweight alignment viewer and editor for large datasets. *Bioinformatics* **30**, 3276–3278 (2014).
53. L. Holm, Benchmarking fold detection by DaliLite v.5. *Bioinformatics* **35**, 5326–5327 (2019).
54. V. B. Chen, W. B. Arendall III, J. J. Headd, D. A. Keedy, R. M. Immormino, G. J. Kapral, L. W. Murray, J. S. Richardson, D. C. Richardson, *MolProbity*: All-atom structure validation for macromolecular crystallography. *Acta Crystallogr. D Biol. Crystallogr.* **66**, 12–21 (2010).
55. M. Sato, T. Arakawa, Y.-W. Nam, M. Nishimoto, M. Kitaoka, S. Fushinobu, Open–close structural change upon ligand binding and two magnesium ions required for the catalysis of *N*-acetylhexosamine 1-kinase. *Biochim. Biophys. Acta.* **1854**, 333–340 (2015).
56. M. D. Hanwell, D. E. Curtis, D. C. Lonie, T. Vandermeersch, E. Zurek, G. R. Hutchison, Avogadro: An advanced semantic chemical editor, visualization, and analysis platform. *J. Chem.* **4**, 17 (2012).
57. A. W. S. da Silva, W. F. Vranken, ACPYPE - AnteChamber PYthon Parser interfacE. *BMC. Res. Notes* **5**, 367 (2012).
58. F. Duarte, P. Bauer, A. Barrozo, B. A. Amrein, M. Purg, J. Åqvist, S. C. L. Kamerlin, Force field independent metal parameters using a nonbonded dummy model. *J. Phys. Chem. B.* **118**, 4351–4362 (2014).
59. K. Lindorff-Larsen, S. Piana, K. Palmo, P. Maragakis, J. L. Klepeis, R. O. Dror, D. E. Shaw, Improved side-chain torsion potentials for the Amber ff99SB protein force field. *Proteins.* **78**, 1950–1958 (2010).
60. K. L. Meagher, L. T. Redman, H. A. Carlson, Development of polyphosphate parameters for use with the AMBER force field. *J. Comput. Chem.* **24**, 1016–1025 (2003).
61. M. J. Abraham, T. Murtola, R. Schulz, S. Páll, J. C. Smith, B. Hess, E. Lindahl, GROMACS: High performance molecular simulations through multi-level parallelism from laptops to supercomputers. *SoftwareX* **1-2**, 19–25 (2015).
62. G. Bussi, D. Donadio, M. Parrinello, Canonical sampling through velocity rescaling. *J. Chem. Phys.* **126**, 014101 (2007).
63. M. Gaus, Q. Cui, M. Elstner, DFTB3: Extension of the self-consistent-charge density-functional tight-binding method (SCC-DFTB). *J. Chem. Theory Comput.* **7**, 931–948 (2012).
64. M. Gaus, A. Goez, M. Elstner, Parametrization and Benchmark of DFTB3 for Organic Molecules. *J. Chem. Theory Comput.* **9**, 338–354 (2013).
65. S. Grimme, J. Antony, S. Ehrlich, H. Krieg, A consistent and accurate *ab initio* parametrization of density functional dispersion correction (DFT-D) for the 94 elements H-Pu. *J. Chem. Phys.* **132**, 154104 (2010).
66. M. Gaus, X. Lu, M. Elstner, Q. Cui, Parameterization of DFTB3/3OB for sulfur and phosphorus for chemical and biological applications. *J. Chem. Theory Comput.* **10**, 1518–1537 (2014).
67. T. Kubař, K. Welke, G. Groenhof, New QM/MM implementation of the DFTB3 method in the gromacs package. *J. Comput. Chem.* **36**, 1978–1989 (2015).
68. A. S. Zlobin, A. O. Zalevsky, Y. A. Mokrushina, O. V. Kartseva, A. V. Golovin, I. V. Smirnov, The preferable binding pose of canonical butyrylcholinesterase substrates is unproductive for echothiophate. *Acta Naturae* **10**, 121–124 (2018).
69. A. Zlobin, Y. Mokrushina, S. Terekhov, A. Zalevsky, T. Bobik, A. Stepanova, M. Aliseychik, O. Kartseva, S. Panteleev, A. Golovin, A. Belogurov Jr., A. Gabibov, I. Smirnov, QM/MM description of newly selected catalytic bioscavengers against organophosphorus compounds revealed reactivation stimulus mediated by histidine residue in the acyl-binding loop. *Front. Pharmacol.* **9**, 834 (2018).

Acknowledgments: We thank D. V. Danilov for support in the eukaryotic expression of AmiN, A. Kotlobay for reagent supply, E. Round for assistance in crystallization, and A. A. Sharapkova for language editing. Computations were carried out using the equipment of the shared research facilities of HPC computing resources at the Lomonosov Moscow State University. **Funding:** This work was supported by grants 19-34-70021 (for S.S.T.) and 18-29-08054 (for I.V.S. and Y.A.M.) from the Russian Foundation for Basic Research, and grant 19-14-00331 from the Russian Science Foundation and NIH (R01 GM104047). **Author contributions:** S.S.T., I.V.S., S.A., and A.G.G. designed the research; S.S.T., Y.A.M., A.S.N., A.Zl., A.Za., G.B., and I.V.S. performed the research; I.A.O., A.A.K., V.A.M., H.J.L., and B.E.T. contributed the new reagent/analytic tools; S.S.T., Y.A.M., A.S.N., A.Zl., A.Za., G.B., A.G., B.E.T., M.W., I.V.S., S.A., and A.G.G. analyzed the data; and S.S.T., Y.A.M., A.Zl., A.Za., A.B.J., I.V.S., S.A., and A.G.G. wrote the paper. **Competing interests:** The authors declare that they have no competing interests. **Data and materials availability:** The crystal structures of AmiN and its complexes with substrates were deposited in PDB (PDB ID: 6SUI, AmiN; 6SV5, AmiN + ATP; 6SUL, AmiN + AMP-PNP + Mg^{2+} + AmiA; 6SUM, hAmiN + AMP-PNP + Mg^{2+} + AmiA; 6SUN, hAmiN + AMP-PNP + Ca^{2+} + AmiA). Crystal structures, initial coordinates for simulations, simulation settings, and metadynamics parameters are available online at https://vsb.fbb.msu.ru/share/amin_kinase/. All data needed to evaluate the conclusions in the paper are present in the paper and/or the Supplementary Materials. Additional data related to this paper may be requested from the authors.

Submitted 25 October 2019
Accepted 16 April 2020
Published 24 June 2020
10.1126/sciadv.aaz9861

Citation: S. S. Terekhov, Y. A. Mokrushina, A. S. Nazarov, A. Zlobin, A. Zalevsky, G. Bourenkov, A. Golovin, A. Belogurov Jr., I. A. Osterman, A. A. Kulikova, V. A. Mitkevich, H. J. Lou, B. E. Turk, M. Wilmanns, I. V. Smirnov, S. Altman, A. G. Gabibov, A kinase bioscavenger provides antibiotic resistance by extremely tight substrate binding. *Sci. Adv.* **6**, eaaz9861 (2020).

Science Advances

A kinase bioscavenger provides antibiotic resistance by extremely tight substrate binding

Stanislav S. Terekhov, Yuliana A. Mokrushina, Anton S. Nazarov, Alexander Zlobin, Arthur Zalevsky, Gleb Bourenkov, Andrey Golovin, Alexey Belogurov, Jr., Ilya A. Osterman, Alexandra A. Kulikova, Vladimir A. Mitkevich, Hua Jane Lou, Benjamin E. Turk, Matthias Wilmanns, Ivan V. Smirnov, Sidney Altman and Alexander G. Gabibov

Sci Adv **6** (26), eaaz9861.
DOI: 10.1126/sciadv.aaz9861